Bull. Mater. Sci., Vol. 39, No. 5, September 2016, pp. 1245–1258. © Indian Academy of Sciences.
DOI 10.1007/s12034-016-1272-1

Effect of height to diameter (*h*/*d*) ratio on the deformation behaviour of Fe–Al_2O_3 metal matrix nanocomposites

PALLAV GUPTA[1], DEVENDRA KUMAR[2,*], A K JHA[3] and OM PARKASH[2]

[1]Department of Mechanical and Automation Engineering, A.S.E.T., Amity University, Noida 201313, Uttar Pradesh, India
[2]Department of Ceramic Engineering, Indian Institute of Technology (Banaras Hindu University), Varanasi 221005, India
[3]Department of Mechanical Engineering, Indian Institute of Technology (Banaras Hindu University), Varanasi 221005, India

MS received 17 March 2015; accepted 21 March 2016

Abstract. **The present paper reports the effect of height to diameter (*h*/*d*) ratio on the deformation behaviour of Fe–Al_2O_3 metal matrix nanocomposites (MMNCs) during bulk processing. Sintered compacts were machined to the required size with different *h*/*d* ratios. Test specimens were subjected to deformation at room temperature under three different interfacial friction conditions such as dry, solid and liquid lubrications. Deformed specimens show a significant improvement in the density and hardness. Results also revealed the formation of a nanosize iron aluminate phase due to reactive sintering, which in turn contributes to grain refinement. Experimental density of the specimens was also verified with the theoretical density using the standard equations. It is expected that the present work will be useful in designing and developing MMNC products with better quality at competitive cost.**

Keywords. **Metal matrix nanocomposites (MMNCs); scanning electron microscopy (SEM); density; hardness; deformation.**

1. Introduction

During last few years, metal matrix nanocomposites (MMNCs) have assumed an important position in industries, as they are being used successfully in a wide range of applications [1]. MMNCs are typically developed engineering materials which employ hard ceramic substance dispersed in a ductile metallic matrix [2]. Several manufacturing techniques such as stir casting, powder metallurgy (P/M), chemical vapour deposition (CVD) and physical vapour deposition (PVD) have been suggested for the synthesis of MMNCs [3–5]. P/M is an attractive process because it avoids large number of sequence of operations, high scrap losses and high energy consumption associated with conventional manufacturing processes such as casting, vapour deposition, etc. [6]. Apart from this, another important factor which plays a vital role in developing quality MMNC products is the particle size and particle size distribution [7]. Components produced by conventional P/M process of compacting metal–ceramic powders have relatively poor mechanical properties due to porosity. However, there are applications which demand high tensile, impact and fatigue strengths. For such applications, the material should have minimum or even no porosity [8]. Bulk processing of metal powder preform is a convenient method of reducing or eliminating the porosity of conventional P/M products. In this new technology, sintered powder preforms are used as the starting materials in metal-forming processes. The mechanical and metallurgical properties of MMNC products manufactured by this new technology are comparable, and in some cases even superior than cast and wrought products [9]. The bulk processing of MMNC preform therefore, has wide industrial applications because of good dimensional accuracy and surface finish of powder components together with the enhancement of their load-bearing capacity.

Gnjidic *et al* [10] reported the compressive strength of Al–SiC metal matrix composites (MMC) synthesized via P/M process using hot isostatic pressing. CW67 aluminum alloy was used as a matrix with SiC particles in three sizes i.e., 0.7, 15 and 33 μm. Nominal SiC particle volume fraction in the composites was 15%. Hot isostatic pressing of the pure metal powder was performed at 723 K for 2 h and for composite mixture at 743 K for 5 h, both under a constant pressure of 35 MPa in an argon atmosphere. It was found that addition of SiC particles increased the yield strength and elastic modulus, while decreasing the ultimate compressive strength and ductility of the CW67 alloy.

Lin *et al* [11] investigated the plastic deformation mechanism of MMC synthesized via P/M process as a factor of bonding strength of interfaces. It was found that strength of the bonds among the matrix particles, particle size distribution, bonding strength between the matrix particles and the reinforcement dominate the mechanical behaviours of MMC. Simple metal and reinforcement powders were simulated as globular particles in the structure. It was found that plastic deformation of MMC under compressive loading

*Author for correspondence (devendra.cer@iitbhu.ac.in)

proceeds by two mechanisms – 'grain deformation' and 'boundaries slip' – according to the bonding strength among different powder particles.

Although a considerable amount of work has been reported recently on the various technological aspects of the aluminum-based composite materials [12–16], unfortunately, the authors have not located any systematic attempts to study the deformation behaviour of Fe–Al_2O_3 MMNCs.

In recent years, our research group has conducted exhaustive investigations on Fe–Al_2O_3 and Fe–ZrO_2 composites synthesized by P/M technique [17–21]. Various properties investigated for these composite include X-ray diffraction (XRD), scanning electron microscopy (SEM), density, hardness, wear, compressive strength and corrosion. It was found from these studies that in both these composite systems, due to reactive sintering, an iron aluminate ($FeAl_2O_4$) and iron zirconium oxide (Zr_6Fe_3O) phases were formed. Due to these phase formations, the various structural, mechanical and electrochemical properties were found to improve. The improvement in the various properties in turn depends on the sintering temperature and time, respectively.

Open die deformation of cylindrical preforms depends on height to diameter (h/d) ratio and interfacial friction conditions because of distribution of stresses during deformation [22]. The present paper reports the effect of h/d ratio on the deformation behaviour of Fe–Al_2O_3 MMNCs during bulk processing. Sintered specimen showed the presence of iron aluminate ($FeAl_2O_4$) phase along with iron (Fe) and alumina (Al_2O_3). Sintered compacts were machined to the required size with different h/d ratios. The test specimens were subjected to deformation under compression at room temperature. Three different interfacial friction conditions such as dry, solid and liquid lubrications were used in the experiment. Deformed specimens show a significant improvement in density and hardness. Micrograph after deformation shows some smaller size particles which are due to the grain growth refinements. Experimental density of samples was also verified with theoretical density using standard equations. It is expected that the present work will be useful in designing and developing MMNC products with better quality at competitive cost.

2. Experimental

2.1 *Preparation of test specimens*

Electrolytic iron metal powder having 99.5% purity and particle size in the range 250–300 mesh (49–58 μm) and active aluminum oxide having particle size of 70–230 mesh (63–210 μm) are used as starting materials for the present composite. All the chemicals used in the present investigation were purchased from Loba Chemie Pvt. Ltd. Composite selected for investigation contains 5% aluminum oxide (Al_2O_3) and 95% iron (Fe), respectively. Mixed powder was compacted at a constant load of seven tons followed by sintering in an argon atmosphere at a temperature of 1100°C for 1 h. After sintering, the compacts were machined on gap or extension type lathe machine so as to achieve the h/d ratio of less than 1 ($h = 9$ mm, $d = 15.2$ mm; $h/d = 0.59$), equal to 1 ($h = 12.8$ mm, $d = 12.8$ mm; $h/d = 1.0$) and greater than 1 ($h = 16$ mm, $d = 11.3$ mm; $h/d = 1.42$). The detailed nomenclature of the specimens sintered at different temperatures and times is discussed in our recent publication [21]. A nomenclature e.g., 5AFe1100(1) is given to a particular specimen in the present case. Here, 5 denotes the percentage of aluminum oxide, A denotes aluminum oxide, Fe denotes iron, 1100 denote the sintering temperature and 1 denotes time of sintering in hour.

2.2 *Phase and microstructure characterization*

Phase determination was done by powder XRD using Rigaku Desktop Miniflex II X-ray diffractometer employing CuKα radiation with Ni-filter. Microstructure along with energy dispersive spectroscopy (EDS) of the undeformed specimen was studied using FEI QUANTA 200 FEG field emission scanning electron microscope (FESEM), whereas the specimen after deformation was studied using Inspect S-50, FP 2017/12 SEM. Specimen for SEM studies before deformation was cut with 12 mm diameter and 5 mm thickness. Specimens were polished using various grades of the emery paper (1/0, 2/0, 3/0 and 4/0), then using alumina gel on polishing cloth and then finally, polished by diamond paste (12, 6 and 0.5 μm). Specimens were also etched with HCl solution for 20 s and then washed and dried in hot air oven.

2.3 *Density, hardness and deformation measurement*

Density of specimen before deformation was determined from the mass and dimensions (i.e., radius and height), whereas after deformation was determined using Archimedes principle. Hardness before and after deformation was measured on a Rockwell Hardness Tester using 1/8″ H scale steel ball indenter having a major loading capacity of 60 kg. Reading of H type indenter was read on the red scale present on dial gauge of the instrument.

Deformation of the specimen was carried up to a load of four tons using a 12 Ton Universal Testing Machine under dry, solid lubricating (graphite powder) and liquid lubricating (Oil-SAE20W40) conditions. Microstructure of the deformed specimens was carried out by cutting the specimens in transverse directions. Bulge profiles were measured considering top, middle and bottom points of the deformed specimens and the same was drawn using AUTOCAD 2008. After the deformation of the nanocomposite specimens, theoretical density was calculated using the following equations [23].

Theoretical density (d_{th}) of the sintered porous composite

$$d_{th} = \rho_{Inst} \times d_f, \tag{1}$$

where d_f is the density of the deformed solid composite found experimentally. Instantaneous relative density (ρ_{Inst})

of the sintered porous composite during compression under pressure (p) is given as

$$\rho_{\text{Inst}} = 1 - \exp\left(\frac{-3p}{2\sigma_c}\right), \tag{2}$$

where σ_c is the yield strength of the sintered porous composite and during compression may be taken as

$$\sigma_c = \frac{\rho_i^k \sigma_o}{1 - 2\eta}, \tag{3}$$

where ρ_i is the initial relative density of the sintered porous composite; σ_o the yield strength of the solid composite taken as 97.3 MPa [18]; k the constant equals to 2 in the yield criteria and η a function of relative density ρ_i only.

Calculated theoretical densities of the specimens have been further discussed in results and discussion section of the present paper.

3. Results and discussion

3.1 *X-ray diffraction*

Figure 1 shows the XRD pattern of representative composite specimen. Peaks of the XRD plot were matched with JCPDS data files of iron and aluminum oxide compounds. It was found from the JCPDS files that the present composition contains iron (Fe), aluminum oxide (Al_2O_3) and iron aluminate ($FeAl_2O_4$) phases, respectively [21,24]. The iron aluminate phase formation takes place due to reactive sintering. All the XRD peaks were indexed.

3.2 *SEM (before deformation)*

To determine the morphology of particles of the present composite system, SEM of a representative nanocomposite specimen was recorded. Figure 2 shows the SEM of the etched surface of specimen 5AFe1100(1) at (a) 100×, (b) 500×, (c) 2000× and (d) 5000× magnifications, respectively. Figure 2a shows the micrograph of the specimen at 100× which shows the circular etched mark on the top surface of the specimen. Same specimen when viewed at 500× magnification (figure 2b) shows highly dense phase composite structure with the presence of uniformly distributed grains of constituent phases. Similarly, figure 2c shows the micrograph of the same specimen at 2000× which shows strong bonding between the various grains with the presence of some submicron size particles between the interstitial sites of the various grains. Figure 2d shows SEM of the present specimen at 5000×, which shows presence of some nanosize particles on the bigger grain.

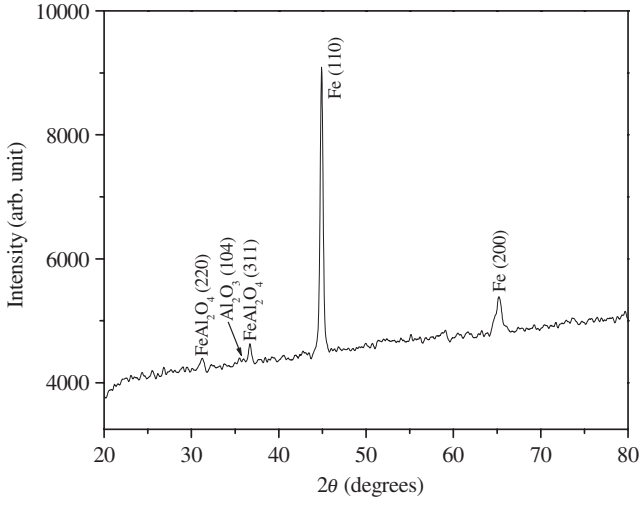

Figure 1. X-ray diffraction pattern of representative composite specimen.

Figure 3 shows the EDS and compositional analysis of etched surface of specimen 5AFe1100(1) (a) full frame, (b) at a point and (c) on a particle. Figure 3a shows the full frame EDS of specimen which shows the presence of iron (Fe) and oxygen (O_2). Oxygen is 09.46 wt% and iron is 90.54 wt%. Figure 3b shows the EDS at a point which shows the presence of oxygen, chlorine and iron. Oxygen is 09.87 wt%, chlorine is 06.97 wt% and iron is 83.16 wt%. Figure 3c illustrates the EDS on a particle which again shows the presence of oxygen and iron. Oxygen is 09.96 wt% and iron is 90.04%.

3.3 *Effect on dimensional changes*

After deformation, diameter and height of all the nanocomposite specimens was measured to determine the changes in their dimensions under different interfacial frictional conditions. Figure 4a shows the variation between % increase in diameter *vs.* h/d ratios for dry, solid lubricant and liquid lubricant conditions. It was found from the results that for $h/d<1$ in dry condition, the % increase in diameter was found out to be 6.31, whereas in solid lubricating condition, it was 5.00 and for the liquid lubricating condition, was 5.65, respectively. For $h/d = 1$, values of % increase in diameter for the dry, solid lubricating and liquid lubricating conditions were found out to be 7.50, 6.71 and 6.71, respectively. Similar measurements for % increase in diameter were carried out for $h/d>1$ under dry, solid lubricant and liquid lubricant conditions, which showed the values to be 6.19, 4.42 and 4.42, respectively. From the above investigations, it was observed that for $h/d<1$, percentage increase in diameter was for the specimen which was deformed in dry state, then for the specimen whose deformation is conducted using liquid lubricant and finally for the specimen whose deformation is done using solid lubricant. Similarly, it can be seen that for $h/d = 1$, the percentage increase in diameter value was highest for specimen whose deformation was conducted in dry state, whereas the values of the solid lubricating specimen and liquid lubricating specimen were same. However, for $h/d>1$, this increase was again highest for the specimen whose test was conducted in dry state and the values were same for the specimen whose test was conducted in solid

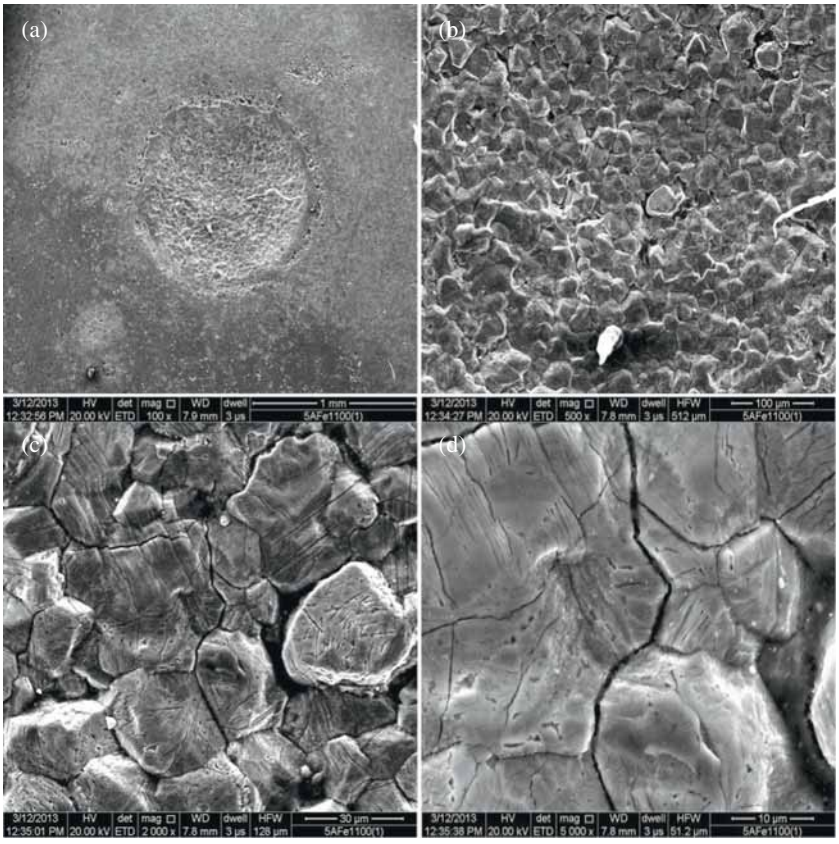

Figure 2. SEM of etched surface of specimen 5AFe1100(1) at (**a**) 100×, (**b**) 500×, (**c**) 2000× and (**d**) 5000× magnifications, respectively.

and liquid lubricating conditions. Therefore, on an overall basis, it can be concluded that the bulging was least in the specimen having h/d ratio > 1 and tested using solid and liquid lubricants. It can also be concluded that the bulging was highest for the specimen having $h/d = 1$ tested in dry condition.

Sintered MMC specimens have porosity and are compressible solids. Decrease in height may or may not result in an equivalent increase in diameter. Deformation behaviour also depends on interfacial friction between plunger and specimen surfaces. Figure 4b shows the variation between % decrease in height *vs.* h/d ratios for dry, solid lubricating and liquid lubricating conditions. It can be seen from the results that for $h/d < 1$ in dry condition, the % decrease in height was found out to be 20.00, whereas for the solid lubricating condition it was found out to be 21.11 and for the liquid lubricating condition it was again found out to be 21.11. Similarly, for the specimens with $h/d = 1$ tested in dry, solid lubricating and liquid lubricating conditions, the % decrease in height was found out to be 25.00, 23.43 and 27.34, respectively. However, for the specimen with $h/d > 1$ tested in dry, solid lubricant and liquid lubricant conditions, the % decrease in height was found out to be 20.62, 17.50 and 18.75, respectively. It can be concluded from the above investigations that for $h/d < 1$, the highest % decrease in height was found out for the specimen which were tested in solid and liquid lubricating conditions and for dry condition it was observed a little less than the prior two. For the $h/d = 1$, the decrease in height was highest for liquid lubricating condition, then for dry condition followed by solid lubricating condition. Finally, for $h/d > 1$, the % decrease in height was highest for specimen subjected to dry condition then for liquid lubricating condition and then for solid lubricating condition. Therefore, on an overall basis, it can be concluded that the % decrease in height value was lowest for the specimen having h/d ratio > 1 and tested in solid lubricating conditions. Highest percentage decrease in height was found for the specimen having $h/d = 1$ and tested in liquid lubricating condition. Figure 5 shows the bulge profile drawn using AUTOCAD 2008 of specimens having (a) $h/d < 1$, (b) $h/d = 1$ and (c) $h/d > 1$ tested under dry condition, respectively. Similar bulge profiles were also drawn for specimens tested under solid and liquid lubricating conditions. These bulge profiles help us to get a comparative idea of deformation characteristics of specimens of different shapes tested under different interfacial conditions. $h/d < 1$, $h/d = 1$ and $h/d > 1$ specimens deformed under dry condition showed reduction in height as 20, 25 and 20.62%, respectively. It can be concluded that the specimen having $h/d > 1$ and tested in solid lubricating condition has least % increase in diameter and % decrease in height values. Best deformation characteristics is shown by the specimen with $h/d = 1$. These have optimum % increase in diameter and % decrease in height.

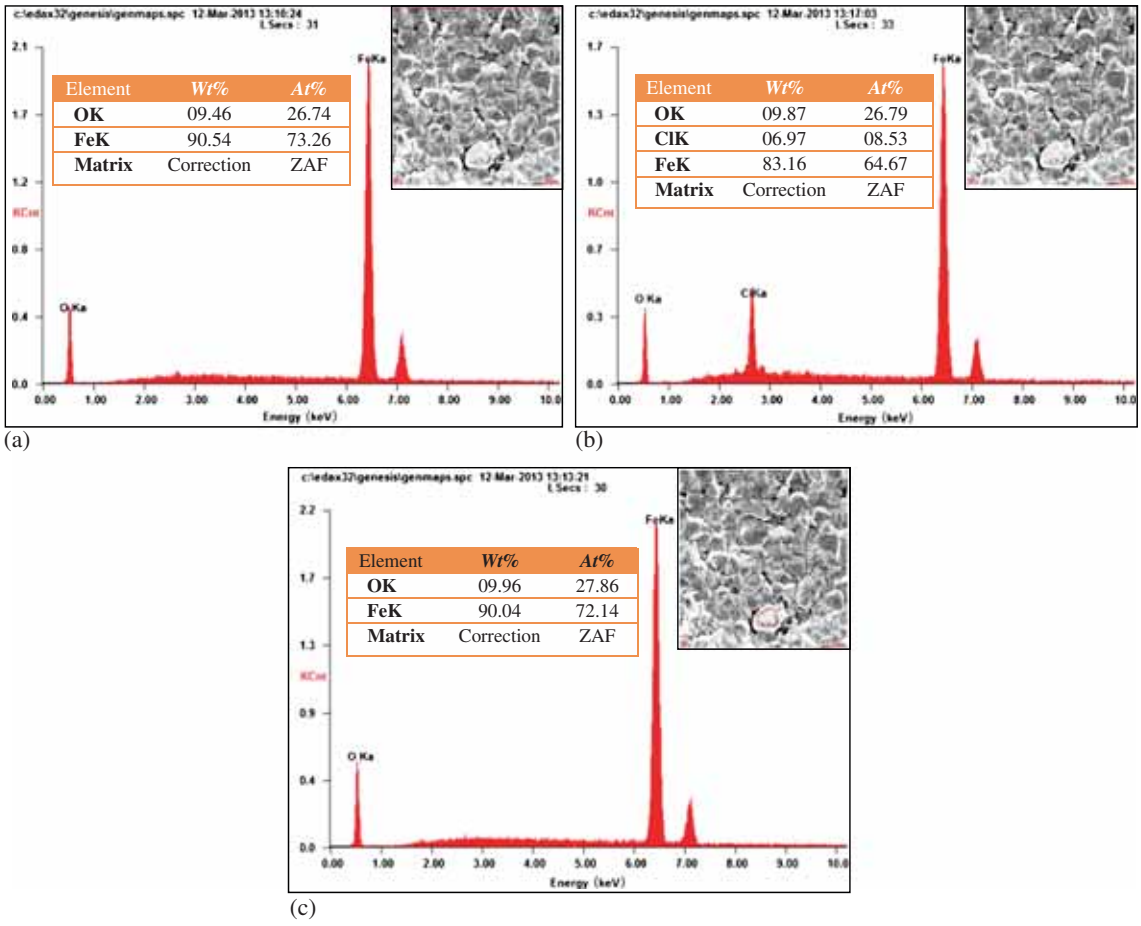

Figure 3. EDAX and compositional analysis of etched surface of specimen 5AFe1100(1): (**a**) full frame, (**b**) at a point and (**c**) on a particle.

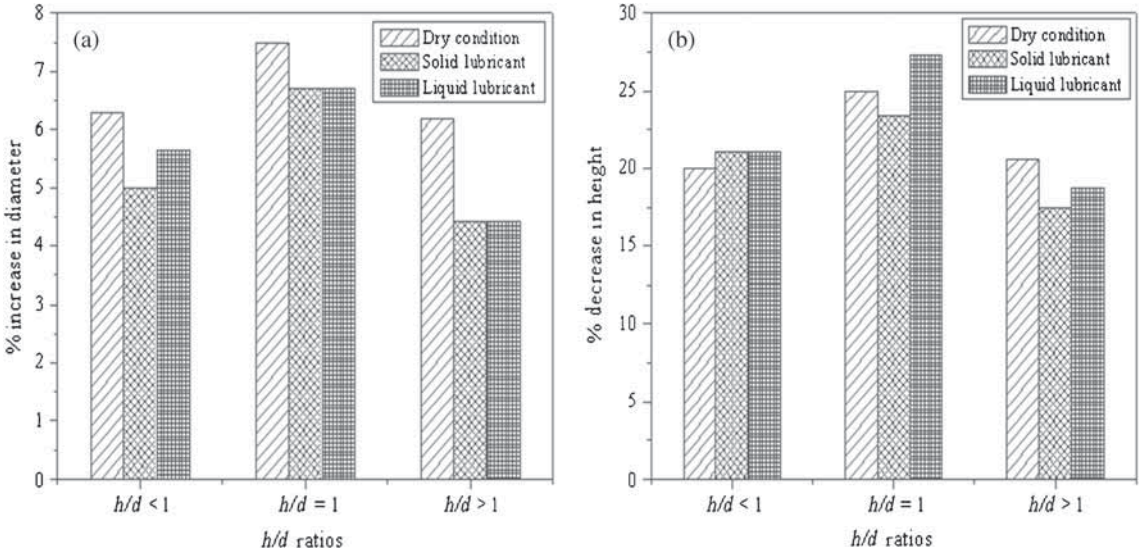

Figure 4. Variation of (**a**) % increase in diameter *vs. h/d* ratios and (**b**) % decrease in height *vs. h/d* ratios for dry, solid lubricant and liquid lubricant conditions.

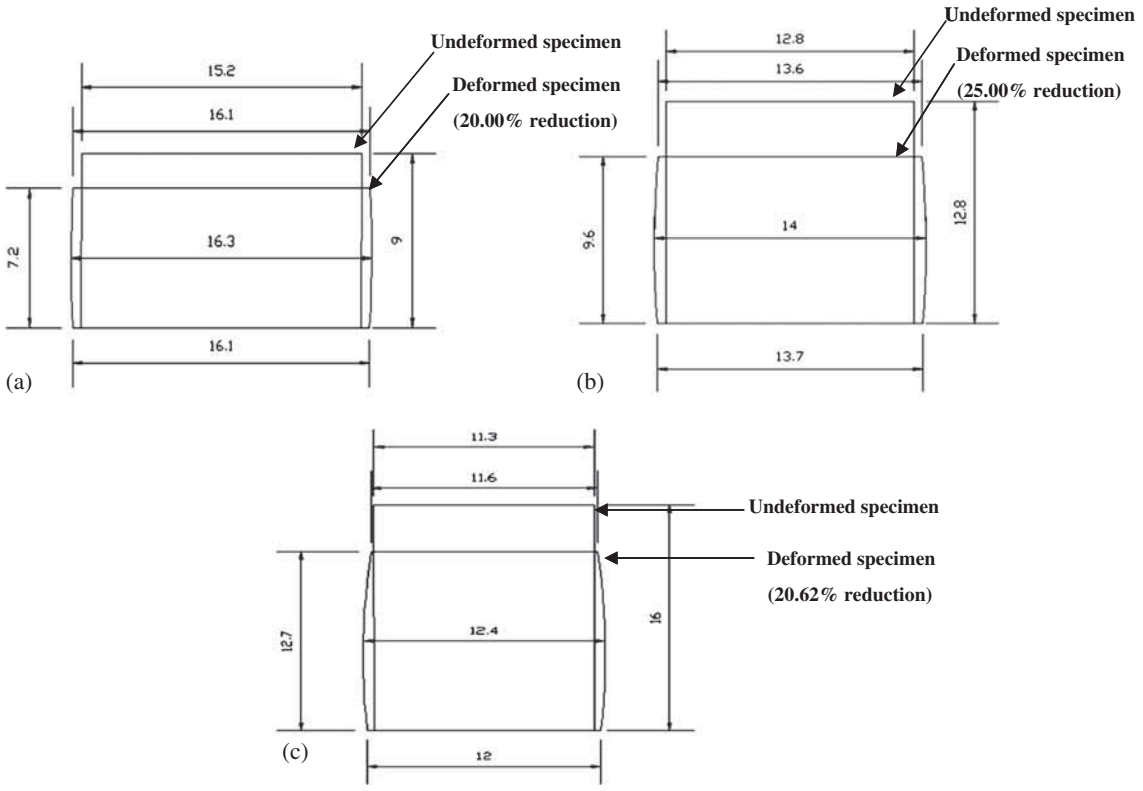

Figure 5. Bulge profile of specimens having (**a**) $h/d < 1$ (**b**) $h/d = 1$ and (**c**) $h/d > 1$ tested under dry condition (all dimensions are in mm).

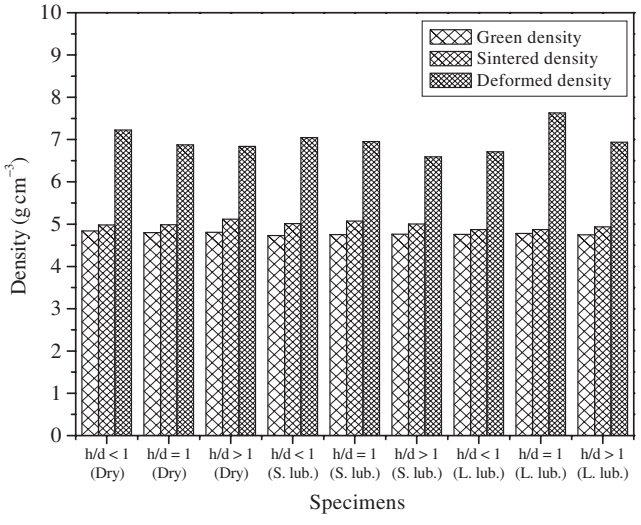

Figure 6. Variation of density *vs.* specimens for green, sintered and deformed co nditions.

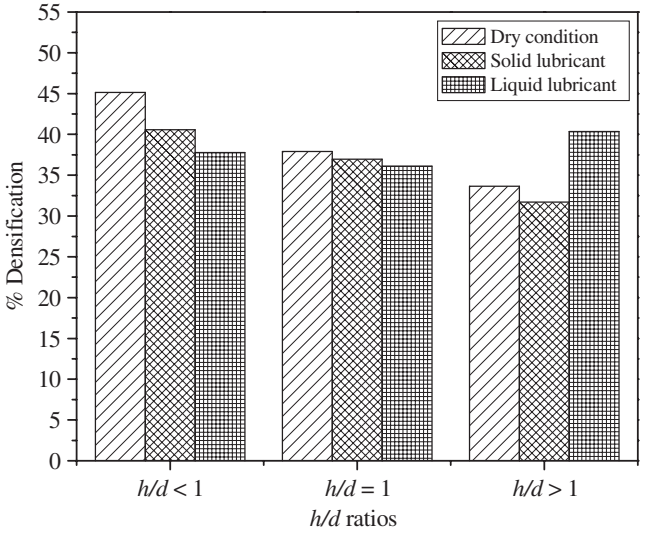

Figure 7. Variations of % densification *vs.* h/d ratios for dry, solid lubricating and liquid lubricating conditions.

3.4 *Effect on density*

Figure 6 shows the difference of density of various specimens for green, sintered and deformed conditions. It was found from the figure that for $h/d < 1$ specimen tested in dry condition, the green density was 4.8388 g cm^{-3}, sintered density was 4.9796 g cm^{-3} and deformed density was 7.2274 g cm^{-3}. For $h/d = 1$ tested in dry condition, specimen has green density 4.7998 g cm^{-3}, sintered density of 4.9867 g cm^{-3} and deformed density of 6.8779 g cm^{-3}. Similarly, the green, sintered and deformed densities of the specimen having h/d ratio > 1 and tested in dry condition were found to be 4.8074, 5.1152 and 6.8376 g cm^{-3}, respectively.

Moreover, the specimens tested with solid lubricant having $h/d < 1$ showed the green density value as 4.7281 g cm^{-3},

sintered density value as 5.0110 g cm^{-3} and deformed density value as 7.0454 g cm^{-3}. With the same lubricant, specimens having $h/d = 1$ showed green, sintered and deformed densities as 4.7500, 5.0748 and 6.9500 g cm^{-3}, respectively.

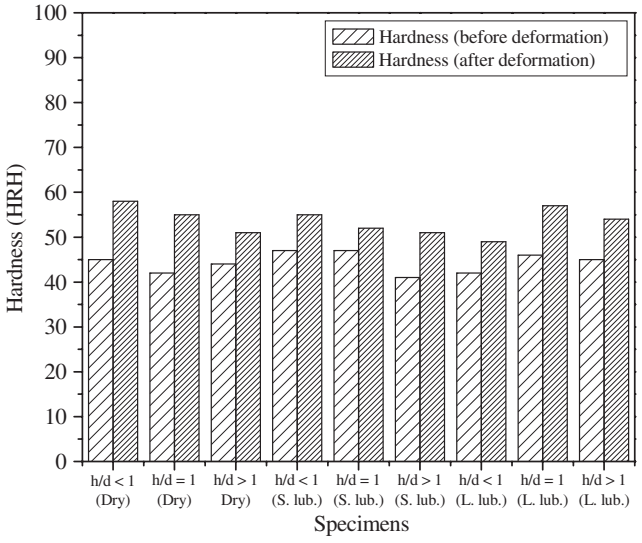

Figure 8. Variations of hardness *vs. h/d* ratios before and after deformation.

Similarly, the specimens having $h/d > 1$ tested with solid lubricant showed green density as 4.7628 g cm^{-3}, sintered density as 5.0032 g cm^{-3} and deformed density as 6.5902 g cm^{-3}.

Finally, for the specimens having $h/d < 1$ tested with liquid lubricants shows the green density as 4.7593 g cm^{-3}, sintered density as 4.8699 g cm^{-3} and deformed density as 6.7101 g cm^{-3}. Specimens having $h/d = 1$ tested with liquid lubricant showed the values of green, sintered and deformed densities as 4.7770, 4.8737 and 7.6283 g cm^{-3}, respectively. For the specimen having $h/d > 1$ and tested with liquid lubricant showed the value of green density as 4.7452 g cm^{-3}, sintered density as 4.9392 g cm^{-3} and deformed density as 6.9336 g cm^{-3}.

It can be concluded from the above results that the density values of sintered specimens are little bit higher than that of green density and deformed densities of the specimens are very much higher than that of the sintered density. The reason for this change in density values can be understood as during the sintering process, there is binder removal and consolidation of the powder particles due to which some voids are being generated and the density is increased only marginally, but after the deformation process those voids which are generated during the sintering are reduced in its size and in number, due to which the overall density of the specimen increases significantly.

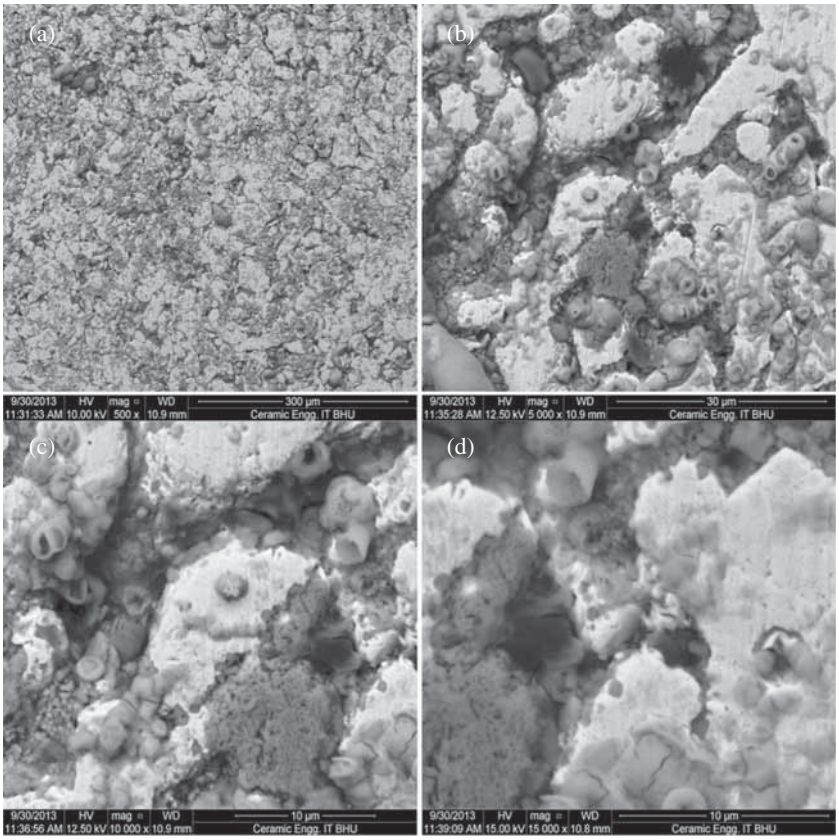

Figure 9. SEM of deformed specimen with $h/d < 1$ in dry state at (**a**) 500×, (**b**) 5000×, (**c**) 10000× and (**d**) 15000×.

Figure 7 shows the variation of % densification *vs. h*/*d* ratios for dry, solid lubricating and liquid lubricating conditions. For $h/d < 1$, percentage densification value for the specimen tested in dry condition shows value of 45.14%, for solid lubricant condition the value is 40.59% and for liquid lubricant the value was found out to be 37.78%. Similarly, for $h/d = 1$, percentage densification value for the specimen tested in dry condition showed a value of 37.92%, in solid lubrication, it was found to be 36.95%, and in liquid lubrication condition, it was found to be 36.11%, respectively. Finally, for $h/d > 1$ tested in dry, solid lubricating and liquid lubricating conditions showed % densification value of 33.67%, 31.71% and 40.37%, respectively. From the above results, it can be concluded that the highest densification was found in the specimens having $h/d < 1$ and tested in dry condition.

3.5 *Effect on hardness*

Figure 8 shows the variation of hardness *vs. h*/*d* ratios before and after deformation for specimens tested under dry, solid lubricating and liquid lubricating conditions. For $h/d < 1$ tested in dry state, the hardness value before deformation was found to be 45 HRH and the hardness number after deformation was found out to be 58 HRH. The specimen having $h/d = 1$ and tested in dry condition has hardness number of 42 HRH before deformation and 55 HRH after deformation. Moreover, the specimen having $h/d > 1$ and tested under dry condition showed hardness number of 44 HRH before deformation and 51 HRH after deformation.

The next spate of specimens was tested with solid lubricating. In this, the specimen having $h/d < 1$ and tested under solid lubricating condition showed a hardness number of 47 HRH before deformation and 55 HRH after deformation. The specimen having $h/d = 1$ and tested with solid lubricant showed hardness number of 47 HRH before deformation and 52 HRH after deformation. Similarly, the specimen having $h/d > 1$ tested with solid lubricant showed hardness number of 41 HRH before deformation and 51 HRH after deformation.

The last slot of the specimens was tested with liquid lubricant. Finally, the specimen having $h/d < 1$ tested with liquid lubrication shows the hardness numbers of 42 HRH and 49 HRH, respectively, before deformation and after deformation. Under same lubricating condition having $h/d = 1$ show the hardness numbers of 46 HRH and 57 HRH, respectively, before deformation and after deformation. For $h/d > 1$ with liquid lubricant, hardness number before deformation was 45 HRH and it was 54 HRH after deformation. On the basis of the above discussions of hardness results, it can be concluded that the highest hardness number for before deformation was found for the cases $h/d < 1$ and $h/d = 1$ tested under solid lubricating condition. The highest hardness number after deformation was found for the specimen having $h/d < 1$ tested under dry condition. Increase in the hardness number of the deformed specimen was due to grain interlocking and reduction in the pore size.

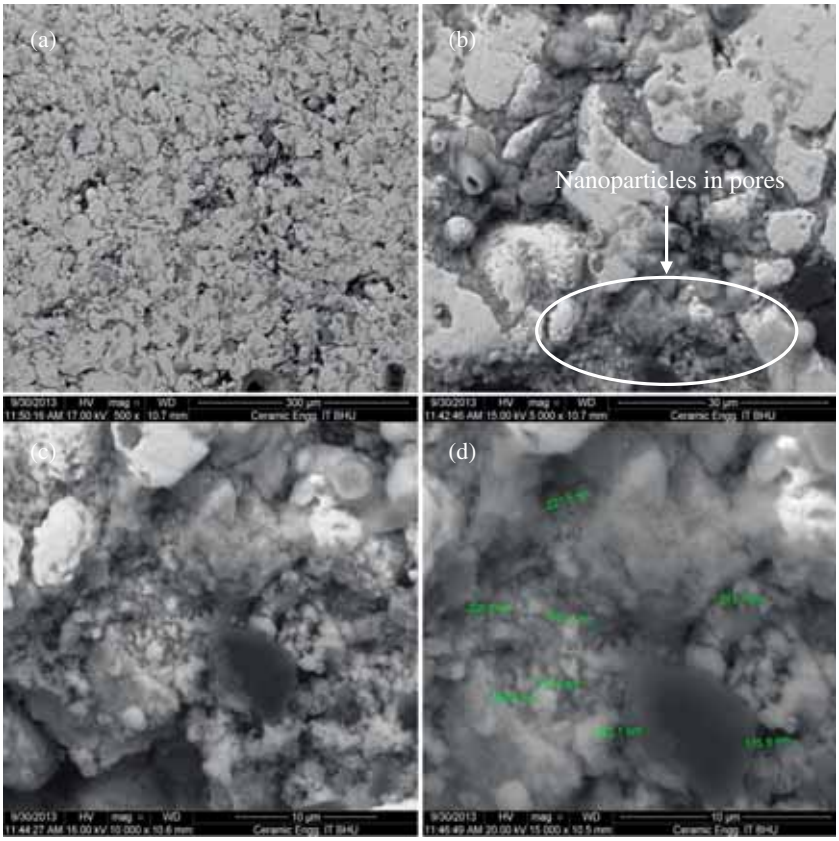

Figure 10. SEM of deformed specimen with $h/d < 1$ in solid lubricating (graphite powder) at (**a**) 500×, (**b**) 5000×, (**c**) 10000× and (**d**) 15000×.

3.6 *SEM (after deformation)*

Figure 9 shows SEM of deformed specimen with $h/d < 1$ in dry state at (a) 100×, (b) 5000×, (c) 10000× and (d) 15000×, respectively. Figure 9a shows the micrograph of the specimen at 500× magnification which shows a highly dense phase structure in comparison with the sintered condition. It also shows a considerable amount of reduction in the intragranular porosity with homogeneously distributed grains of constituent phases. Figure 9b shows SEM of the same specimen at 5000× magnification which discusses the entrapment of fine nanosize iron aluminate particles in the intragranular pores of the specimen. Due to this filling of the nanoparticles in the pores of the specimen, it achieves much more densification. It also shows bigger iron grains of size 5–10 μm. Figure 9c shows SEM of the same specimen at 10000× magnification which reveals the strong bonding between the various particles of the constituent phases. This bonding among the various particles is formed due to the deformation process. The last micrograph shows the microscopic image of specimen at 15000× (figure 9d). The present SEM image also reveals no cracks on the inner surface of the specimen.

Figure 10 shows SEM of deformed specimen with $h/d < 1$ in solid lubricating (graphite powder) at (a) 500×, (b) 5000×, (c) 10000× and (d) 15000×. Figure 10a shows the micrograph of the specimen at 500× magnification which shows a highly dense phase structure in comparison to the sintered condition. This micrograph is denser in comparison to the specimen deformed in dry condition. It also shows a considerable amount of reduction in the intragranular porosity with the presence of homogeneously distributed grains of constituent phases. Figure 10b shows SEM of the same specimen at 5000× magnification which discusses the entrapment of fine nanosize iron aluminate particles in the intragranular pores of the specimen. Owing to this filling of the nanoparticles in the pores of the specimen, the specimen achieves much more densification. The same micrograph also shows bigger size grains of 5–10 μm. Figure 10c shows SEM of the same specimen at 10000× magnification which reveals strong bonding between the various particles of constituent phases. This bonding among the various particles is formed due to the deformation process. Owing to the deformation process, the grain interlocking and filling of the pores with the nanosize particles can be seen. The last micrograph shows the electron microscopic image of the specimen at 15000× (figure 10d). The present SEM image reveals no cracks on inner surface of the specimen as well as it shows nanosize particles in the range of 200–300 nm.

Figure 11 shows the SEM of deformed specimen with $h/d < 1$ in liquid lubricating (oil) at (a) 500×, (b) 5000×, (c) 10000× and (d) 15000×. Figure 11a shows the micrograph of the specimen at 500× magnification which shows a

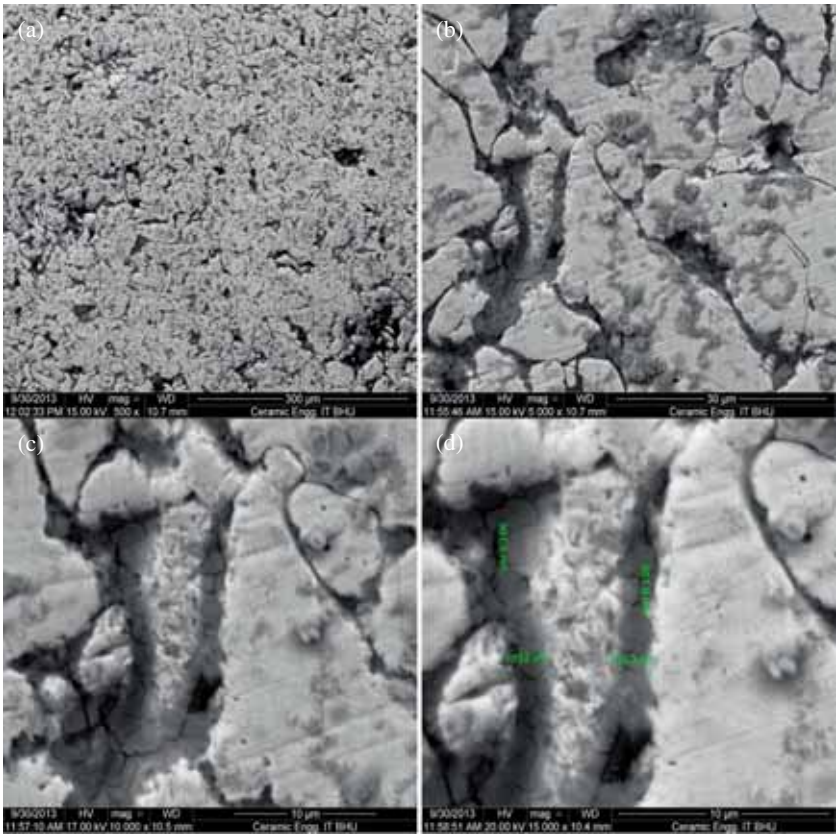

Figure 11. SEM of deformed specimen with $h/d < 1$ in liquid lubricating (oil) at (**a**) 500×, (**b**) 5000×, (**c**) 10000× and (**d**) 15000×.

highly dense phase structure in comparison with the sintered condition. This micrograph is denser in comparison with the specimen deformed under dry and solid lubricating condition. The same micrograph also shows a considerable amount of reduction in the intragranular porosity. Similar to the previous two specimens, this also shows the homogeneously distributed grains of constituent phases. Figure 11c shows the SEM of the same specimen at 5000× magnification which discusses the entrapment of fine nanosize iron aluminate particles in the intragranular pores of the specimen. Due to this filling of the nanoparticles in the pores of the specimen, it achieves much more densification. Micrograph also shows bigger size grains of 5–10 μm. Figure 11c shows the SEM of the same specimen at 10000× magnification which reveals the strong bonding between the various particles of the constituent phases. This bonding among the various particles is formed due to the deformation process. The last micrograph shows the microscopic image of the specimen at 15000× (figure 11d). The present SEM image also reveals no cracks on the inner surface of the specimen.

Figure 12 shows the SEM images of deformed specimen with $h/d = 1$ in dry state at (a) 500×, (b) 5000×, (c) 10000× and (d) 30000× after cutting the specimen in the transverse direction. The micrograph of the specimen at 500× (figure 12a) shows a higher density amongst the constituent particles in comparison with the micrographs taken before the deformation. It was also observed that the porosity factor was almost negligible due to the closer association of the intergranular and intragranular porosity during the deformation process. The same micrograph when viewed at 5000× magnification (figure 12b) shows the plastically deformed grains of the various constituent phases. The plastically deformed grains severely undergo bonding, resulting in strengthening the mechanism caused by the action of Al_2O_3 reinforcement and by nanosize iron aluminate phase. It also shows the conjunction of different particles or flake type arrangement of the constituent phases formed during the plastic deformation of composites. It was also observed that during the deformation process, each grain is trying to deform homogeneously in conformity with the deformation of the specimen as a whole, thus causing constraints imposed by continuity and considerable differences in the deformation between neighbouring grains and within each grain. Flake type arrangement of length 5–8 μm and width 10–12 μm along with some nanosize grains formed due to the deformation process which can also be seen in the present micrograph. It is also seen that some nanoparticles lie on the intraparticle's site of the composite structure. The micrograph of the same specimen at 10000× magnification is shown in figure 12c, which illustrates some submicron size nanorods of the iron aluminate phase formed during the deformation process. Finally, the micrograph at 30000× magnification

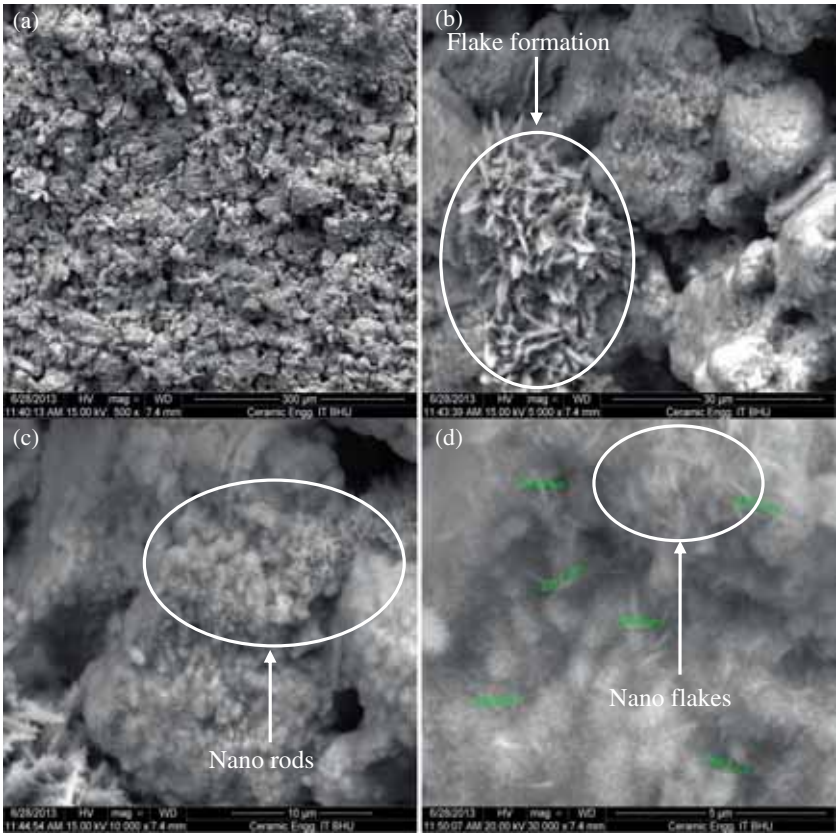

Figure 12. SEM of deformed specimen with $h/d = 1$ in dry state at (**a**) 500×, (**b**) 5000×, (**c**) 10000× and (**d**) 30000×.

(figure 12d) illustrates the formation of some nanosize rods of length varying from 60 to 600 nm size range. The same micrograph also illustrates the presence of some nanosize particles of iron aluminate.

Figure 13 shows the SEM images of deformed specimen with $h/d = 1$ tested in solid lubricating (graphite powder) condition at (a) 500×, (b) 5000×, (c) 10000× and (d) 30000× after cutting the specimen in transverse direction. Micrograph of the nanocomposite specimen at 500× magnification (figure 13a) shows a highly dense phase structure in comparison with the micrograph of specimen before deformation. It shows basically two types of grain geometry: (1) first class of grains are settled in a uniform manner and (2) the group of grains which are making a chain type structure amongst each other. These two types of arrangements are formed due to the plastic deformation of the constituent phases. During the plastic deformation when load is removed, some particles remain as it is and some regain their original shape and size thus forming two types of geometries as discussed in point 1 and 2, respectively. An inner view of the settled bed of grains is visible more clearly in figure 13c which shows the micrograph of the same specimen at 10000×, and shows some microcracks on the site of the grains. It also shows a highly densified structure of the inner bed settled location with microcracks. SEM image of the same specimen at 30000× is shown in figure 13d, which shows a web type structure having several threads of iron aluminate phase formed during the deformation process. The effect is quite severe due to which a large number of nanothreads are formed and can be viewed very clearly in this micrograph.

Figure 14 shows the SEM of deformed specimen with $h/d > 1$ in dry state at (a) 500×, (b) 5000×, (c) 10000× and (d) 15000×, respectively. The micrograph at 500× magnification (figure 14a) shows a highly dense phase composite structure with the presence of negligible amount of porosity. Micrograph at 5000× magnification as illustrated in figure 14b shows the closely placed intergranular pores which is due to the deformation action. It also shows the pores which are present on the grains i.e., intragranular pores which are also reduced in size due to the deformation action. It also shows the presence of some nanosize particles of iron aluminate phase on the intragranular sites of the nanocomposite specimen. The presence of these nanosize particles can be seen much more clearly in the micrographs taken at 10000× (figure 14c) and 15000× (figure 14d) magnifications.

Figure 15 shows the SEM images of deformed specimen with $h/d > 1$ in solid lubricating (graphite powder) state at (a) 500×, (b) 5000×, (c) 10000× and (d) 15000× magnifications, respectively. Micrograph at 500× (figure 15a) illustrates the formation of dense phase structure with small amount of pores. The same specimen when viewed at 5000× magnification (figure 15b) shows a smaller fraction of pores in comparison with the sintered specimen. The reduction in the pores can be attributed to the deformation action. It

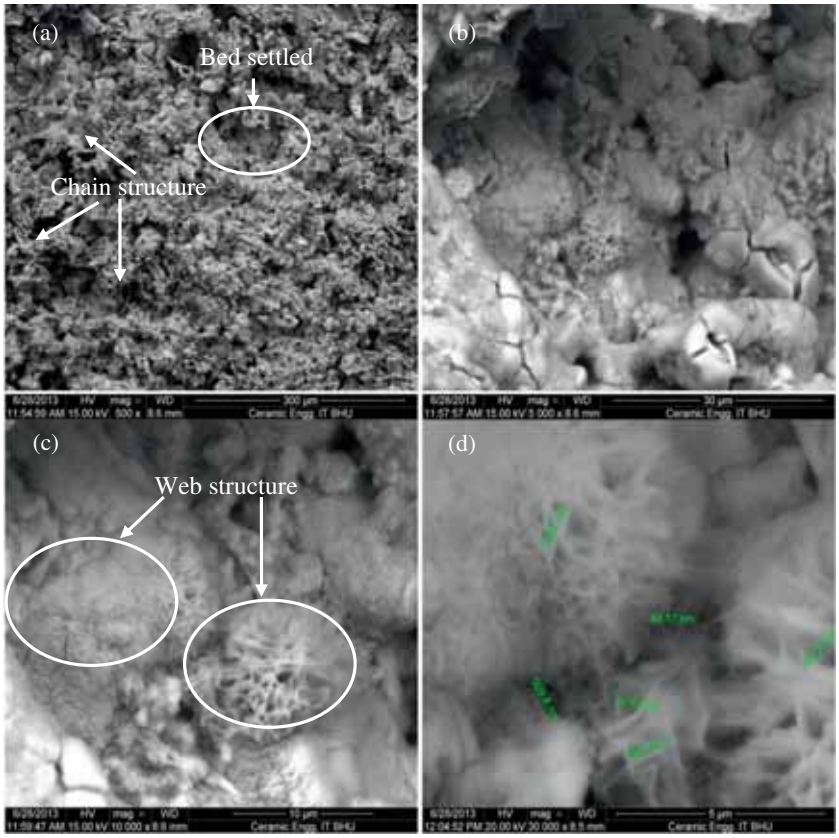

Figure 13. SEM of deformed specimen with $h/d = 1$ in solid lubricating (graphite powder) state at (**a**) 500×, (**b**) 5000×, (**c**) 10000× and (**d**) 30000×.

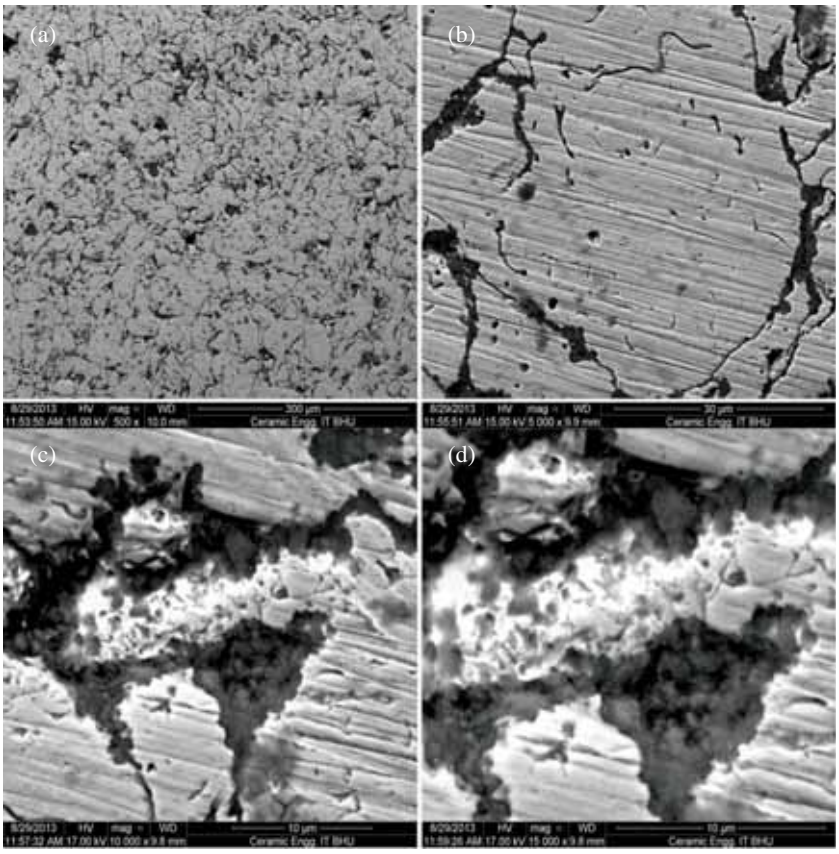

Figure 14. SEM of deformed specimen with $h/d > 1$ in dry state at (**a**) 500×, (**b**) 5000×, (**c**) 10000× and (**d**) 15000×.

also reveals that the intergranular as well as the intragranular porosity present on the specimen surface are completely removed due to this deformation process. It also reveals the reduction in grain size. Figure 15c shows the micrograph of the same specimen at 10000× which reveals that due to the deformation process not only the grain size reduction takes place, but the closer association of the grains is also occurring. It is very much interesting to note from figure 15d, which is the micrograph of the same specimen at 15000×, that even after the deformation process no micro cracks were generated on the specimen surface. It could be concluded from the above micrographs that the closer association of the intergranular and intragranular pores is due to the deformation process. It is also evident to state that the nanosize particles which were subsided in the pores of the specimen moved up to the surface of the composite specimen after deformation process due to which the various factors such as density and hardness were found to increase. The density and hardness numbers were improved in comparison to the sintered values.

On the basis of the above results, it can be concluded that there is a plastic deformation in the nanocomposite specimens under the action of the compressive stresses. Depending on the compressive stresses, strength of the matrix and bonding strength of the grain boundaries, deformation can take place in two types of modes; (a) grain deformation and (b) boundary slip. 'Grain deformation' occurs when the bonding strength at the boundaries among the metal matrix composite particles exceeds that of the matrix particles and compressive stresses exceed yield strength of matrix, i.e., the matrix particles deform plastically first. Second phenomenon is the 'boundary slip' which occurs when the bonding strength of the grain boundaries is lower than the strength of the matrix particles. Under compressive loading, when the shear stress exceeds the shear strength of the grain boundaries, then the shear stress induced at the boundaries among the particle causes boundary slip or sliding. Large scoring marks can be seen in the microstructure of the deformed specimens due to the boundary slip.

In the present case, due to reactive sintering, there is an iron aluminate phase formation which gets deformed and fills in the porosity of the nanocomposite specimens. When the bonding strength between matrix and reinforcement phase is strong and there is also a reactive phase, then by the effect of compressive stresses, a strong web and flake type structures are formed. In such type of cases, plastic deformation is simultaneously caused by the 'boundary slip' whereas 'grain deformation' mechanisms. 'Boundary slip' occurs among the reinforcing particles and the matrix particles whereas 'grain deformation' occurs among the reactive particles ($FeAl_2O_4$). Under such conditions, there is an increase in the strength of the composite [25].

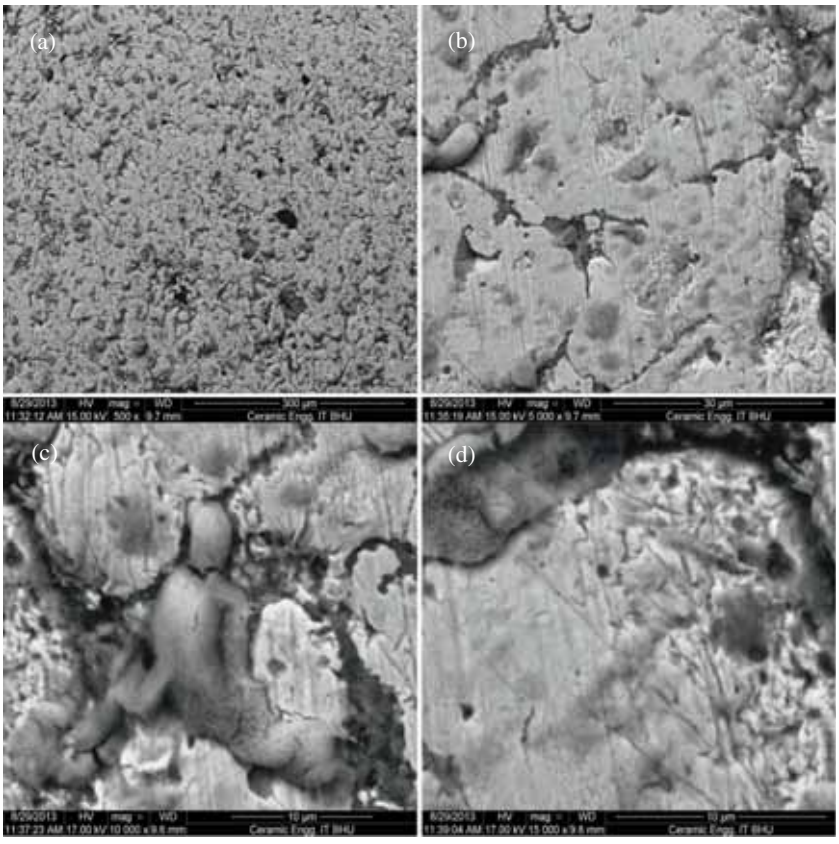

Figure 15. SEM of deformed specimen with $h/d > 1$ in solid lubricating (graphite powder) state at (**a**) 100×, (**b**) 5000×, (**c**) 10000× and (**d**) 15000×.

Table 1. Theoretical and experimental densities of the deformed specimens.

Sample no.	ρ_c (g cc^{-1})	d_{sc} (g cc^{-1})	ρ_i	η	σ_o (MPa)	p (MPa)	σ_c (MPa)	ρ_{Inst}	d_{exp} (g cc^{-1})	d_f (g cc^{-1})
$h/d < 1$ (dry)	4.9796	7.5	0.7	0.1273	97.30	196.48	63.96	0.9900	7.2274	7.1551
$h/d < 1$ (grap.)	5.0110	7.5	0.7	0.1273	97.30	201.45	63.96	0.9911	7.0454	6.9826
$h/d < 1$ (oil)	4.8699	7.5	0.7	0.1273	97.30	198.94	63.96	0.9910	6.7101	6.6497
$h/d = 1$ (dry)	4.9867	7.5	0.7	0.1273	97.30	275.35	63.96	0.9984	6.8779	6.8668
$h/d = 1$ (grap.)	5.0748	7.5	0.7	0.1273	97.30	283.63	63.96	0.9987	6.9500	6.9409
$h/d = 1$ (oil)	4.8737	7.5	0.7	0.1273	97.30	283.63	63.96	0.9987	7.6283	7.6183
$h/d > 1$ (dry)	5.1151	7.5	0.7	0.1273	97.30	378.49	63.96	0.9998	6.8376	6.8362
$h/d > 1$ (grap.)	5.0032	7.5	0.7	0.1273	97.30	372.04	63.96	0.9998	6.5902	6.5888
$h/d > 1$ (oil)	4.9392	7.5	0.7	0.1273	97.30	372.04	63.96	0.9998	6.9336	6.9322

The value of stress during the deformation process in all the specimens is found to be highest at the centre and it reduces as it moves towards the outer periphery. In $h/d < 1$ and $h/d = 1$, the value of stress is greater than that of the yield strength value, therefore, there is grain deformation as well as grain boundary slipping in specimens under all the interfacial friction conditions. For $h/d > 1$, the value of stress is less than the yield strength therefore, there is only boundary slip in the specimen deformed under all the frictional conditions. Microstructures of specimens having $h/d < 1$ and $h/d = 1$ show the presence of nano iron aluminate phase in the intergranular and intragranular pores of the specimen. Microstructures of specimens having $h/d > 1$ shows the presence of the sliding marks on the specimen surface due to the effect of grain boundary sliding.

3.7 *Theoretical analysis*

Table 1 depicts the theoretical and experimental densities of the sintered porous composite samples during compression. For all the samples, initial relative density of the composite, ρ_i is taken as 0.7. Yield strength of the composite during

compression σ_c is calculated using equation (2). Using the value of σ_c and equation (1), instantaneous relative density of the composite, ρ_{Inst} is calculated. Finally, theoretical density d_f is calculated using equation (3).

Specimen having $h/d < 1$ and tested in dry condition showed experimental density as 7.2274 g cc^{-1} and theoretical density as 7.1551 g cc^{-1}, whereas the same specimen tested with graphite as lubricant showed experimental density as 7.0454 g cc^{-1} and theoretical density as 6.9826 g cc^{-1} and with oil as the lubricant showed the experimental density as 6.7101 g cc^{-1} and theoretical density as 6.6497 g cc^{-1}. In the similar manner, specimen having $h/d = 1$ and tested in dry condition showed experimental density as 6.8779 g cc^{-1} and theoretical density as 6.8668 g cc^{-1}, whereas when the same specimen was tested with graphite as lubricant showed experimental density as 6.9500 g cc^{-1} and theoretical density as 6.9409 g cc^{-1} and when tested with oil as the lubricant showed the experimental density as 7.6283 g cc^{-1} and theoretical density as 7.6183 g cc^{-1}. The last slot of specimen was fabricated with $h/d > 1$, specimen tested with dry condition showed experimental density as 6.8376 g cc^{-1} and theoretical density as 6.8362 g cc^{-1}, specimens tested with graphite as lubricant showed experimental density as 6.5902 g cc^{-1} and theoretical density as 6.5888 g cc^{-1}, whereas the specimen tested with oil as the lubricant showed experimental density as 6.9336 g cc^{-1} and theoretical density as 6.9322 g cc^{-1}. From the above discussion, it can be concluded that the instantaneous relative density of all the specimens lies between 0.9900 and 0.9998 and also the theoretical deformed densities of the nanocomposite specimens were in close proximity with that of the experimental densities.

4. Conclusions

The feasibility of bulk processing of Fe–Al_2O_3 MMNCs is demonstrated in the present work. Test specimens having different height to diameter (h/d) ratios have been deformed at room temperatures under different interfacial friction conditions. The deformation patterns of different specimens were studied and it is found that the dry specimens show more bulging than the lubricated ones. The test specimen show more surface movement on top surface than the bottom surface in all the deforming conditions. A significant improvement in density and hardness is observed in all the deformed test specimens. All specimens show no cracking due to bulging at the equatorial free surface up to 25% reduction.

Further, XRD and SEM results have also been reported in this paper. The deformed specimen show a significant improvement in grain size structure and few micrographs even show deformation of nanosize particles in the specimen. The deformation of nanosize iron aluminate has also been revealed in few micrographs. Experimental and theoretical densities were found to be in close proximity with each other. It is expected that the outcome of these investigations will be helpful in developing MMNCs possessing better mechanical and metallurgical properties and also producing quality MMNC products economically.

References

[1] Kaczmar J W, Pietrzak K and Wlosinski W 2000 *J. Mater. Process. Technol.* **106** 58

[2] Ralph B, Yuen H C and Lee W B 1997 *J. Mater. Process. Technol.* **63** 339

[3] Miracle D B 2005 *Comp. Sci. Tech.* **65** 2526

[4] Rosso M 2006 *J. Mater. Process. Technol.* **175** 364

[5] Harrigan Jr W C 1998 *Mater. Sci. Eng. A* **244** 75

[6] Moustafa S F, Hamid Z A and Abd-Elhay A M 2002 *Mater. Lett.* **53** 244

[7] Pournaderi S, Mahdavi S and Akhlaghi F 2012 *Powder Technol.* **229** 276

[8] Chen S H and Wang T C 2002 *Acta Mech.* **157** 113

[9] Sutradhar G, Jha A K and Kumar S 1995 *J. Mater. Process. Technol.* **51** 369

[10] Gnjidic Z, Bozic D and Mitkov M 2001 *Mater. Charact.* **47** 129

[11] Lin Y C, Li H C, Liou S S and Shie M T 2004 *Mater. Sci. Eng. A* **373** 363

[12] Rahimian M, Ehsani N, Parvin N and Baharvandi H R 2009 *J. Mater. Process. Technol.* **209** 5387

[13] Zhang D L, Brindley C and Cantor B 1993 *J. Mater. Sci.* **28** 2267

[14] Sahu K and Jha A K 2012 *Int. J. Manuf. Technol. Res.* **8** 1

[15] Mondal M K, Biswas K and Maity J 2013 *J. Mater. Engg. Perform.* **22** 3364

[16] Shamanian M, Mohammadnezhad M and Szpunar J 2014 *J. Mater. Eng. Perform.* **23** 3152

[17] Gupta P, Kumar D, Quraishi M A and Parkash O 2013 *Adv. Sci. Eng. Med.* **5** 366

[18] Gupta P, Kumar D, Parkash O and Jha A K 2013 *Bull. Mater. Sci.* **36** 859

[19] Gupta P, Kumar D, Parkash O and Jha A K 2014 *Proc. Inst. Mech. Eng., Part J.: J. Eng. Tribol.* **228** 362

[20] Jha P, Gupta P, Kumar D and Parkash O 2014 *J. Compos. Mater.* **48** 2107

[21] Gupta P, Kumar D, Parkash O and Jha A K 2014 *J. Compos.* Art. ID 145973, 1

[22] Kobayashi S 1970 *ASME J. Manuf. Sci. Eng.* **92** 391

[23] Jha A K and Kumar S 1988 *I. Inst. Engs.* **68** 110

[24] Konopka K and Ozieblo A 2001 *Mater. Charact.* **46** 125

[25] Rabiei A, Vendra L and Kishi T 2008 *Composites: Part A* **39** 294